

A *NUSTAR* OBSERVATION OF THE REFLECTION SPECTRUM OF THE LOW MASS X-RAY BINARY 4U 1728-34

CLIO C. SLEATOR¹, JOHN A. TOMSICK¹, ASHLEY L. KING², JON M. MILLER³, STEVEN E. BOGGS¹, MATTEO BACHETTI^{4,5}, DIDIER BARRET^{4,5}, JÉRÔME CHENEVEZ⁶, FINN E. CHRISTENSEN⁶, WILLIAM W. CRAIG^{7,8}, CHARLES J. HAILEY⁸, FIONA A. HARRISON⁹, FARID RAHOUI^{10,11}, DANIEL K. STERN¹², DOMINIC J. WALTON⁹, WILLIAM W. ZHANG¹³

Submitted to ApJ

ABSTRACT

We report on a simultaneous *NuSTAR* and *Swift* observation of the neutron star low-mass X-ray binary 4U 1728-34. We identified and removed four Type I X-ray bursts during the observation in order to study the persistent emission. The continuum spectrum is hard and well described by a black body with $kT = 1.5$ keV and a cutoff power law with $\Gamma = 1.5$. Residuals between 6 and 8 keV provide strong evidence of a broad Fe $K\alpha$ line. By modeling the spectrum with a relativistically blurred reflection model, we find an upper limit for the inner disk radius of $R_{\text{in}} \leq 2R_{\text{ISCO}}$. Consequently we find that $R_{\text{NS}} \leq 23$ km, assuming $M = 1.4M_{\odot}$ and $a = 0.15$. We also find an upper limit on the magnetic field of $B \leq 2 \times 10^8$ G.

Subject headings: accretion, accretion disks, X-rays: binaries, stars: neutron

1. INTRODUCTION

Iron emission lines with energies from 6.4 to 7.1 keV have been detected in some neutron star X-ray systems. These lines are most likely due to the fluorescent $K\alpha$ transition of iron, caused by the reflection of hard X-ray emission onto an area of the accretion disk close to the compact object (Fabian et al. 1989). Relativistic and Doppler effects distort the profile of the line, broadening it significantly and skewing it to low energies (Miller 2007; Reynolds & Nowak 2003). From this unique shape, one can measure interesting properties of the accretion disk, including its inner radius. An upper limit for the neutron star radius can thus be inferred from the reflection spectrum, which is critical to understanding the neutron star equation of state (Lattimer & Prakash 2007; Cackett et al. 2010).

4U 1728-34 is a neutron star low-mass X-ray binary (LMXB) of the atoll class (Lewin et al. 1976; Hasinger & van der Klis 1989), with an estimated distance of 4.1-5.1 kpc (Di Salvo et al. 2000; Galloway et al. 2003). It exhibits Type-I X-ray bursts caused by thermonuclear burning on the stellar surface (Galloway et al. 2010). From burst oscillations, Strohmayer et al. (1996) measured a spin frequency of 363 ± 6

Hz.

A broad emission line at 6.7 keV has been detected in several spectral analyses of 4U 1728-34 performed with satellites such as *XMM-Newton* (Ng et al. 2010; Egron et al. 2011), *INTEGRAL* (Tarana et al. 2011), *RXTE* (Piraino et al. 2000; Seifina & Titarchuk 2011) and *BeppoSAX* (Di Salvo et al. 2000; Piraino et al. 2000; Seifina & Titarchuk 2011). The continuum spectrum is generally composed of a soft component described as thermal emission from the stellar surface or accretion disk, and a hard component described as Comptonization or thermal Brehmsstrahlung.

The *Nuclear Spectroscopic Telescope Array* (*NuSTAR*; Harrison et al. 2013) has been successful in revealing iron $K\alpha$ lines and reflection spectra in neutron stars (e.g. Miller et al. 2013, Degenaar et al. 2015, King et al. 2016). In this work we analyze a coordinated *NuSTAR* and *Swift* observation of 4U 1728-34 in an effort to further constrain its reflection spectrum and thus the neutron star radius.

2. OBSERVATIONS AND DATA REDUCTION

NuSTAR observed 4U 1728-34 on 2013 October 1 for 33.5 ks (Obs ID 80001012002; Figure 1). The data were processed with the *NuSTAR* Data Analysis Software (*NuSTARDAS*) version 1.4.1 and CALDB 20150702, resulting in 27 ks of net exposure time. We extracted spectra from the FPMA and FPMB focal planes using a circular region with a $180''$ radius centered at the source position. We used a $671'' \times 114''$ rectangular background region centered $388''$ away from the source position. At 5 keV, the ratio of source count rate to background count rate is 200, and, at 50 keV, this ratio is 3, indicating that the spectrum is not very sensitive to the background estimate. Due to a known shift in gain offset that has not been properly accounted for in the current response files used for the reduction in this paper, we restrict our analysis to the 4.5-78.4 keV band¹⁴.

An observation (ObsID 00080185001) of 4U 1728-34 was made with the *Swift* (Gehrels et al. 2004) X-ray telescope (XRT; Burrows et al. 2005) near the beginning of the *NuSTAR* observation (see Figures 1 and 3). The XRT was operated in Windowed Timing mode to avoid photon pile-up. Although

¹⁴ Confirmed by *NuSTAR* instrument team (Kristin Madsen, private communication)

¹ Space Sciences Laboratory, 7 Gauss Way, University of California, Berkeley, CA 94720-7450, USA

² KIPAC, Stanford University, 452 Lomita Mall, Stanford, CA 94305, USA

³ Department of Astronomy, The University of Michigan, 500 Church Street, Ann Arbor, MI 48109-1046, USA

⁴ Université de Toulouse, UPS-OMP, Toulouse, France

⁵ CNRS, Institut de Recherche en Astrophysique et Planetologie, 9 Av. colonel Roche, BP 44346, F-31028, Toulouse cedex 4, France

⁶ DTU Space, Technical University of Denmark, Elektrovej 327-328, Lyngby, DK

⁷ Lawrence Livermore National Laboratory, Livermore, CA

⁸ Columbia Astrophysics Laboratory and Department of Astronomy, Columbia University, 550 West 120th Street, New York, NY 10027, USA

⁹ Cahill Center for Astronomy and Astrophysics, California Institute of Technology, Pasadena, CA 91125, USA

¹⁰ European Southern Observatory, Karl Schwarzschild-Strasse 2, D-85748 Garching bei M \ddot{u} nchen, Germany

¹¹ Department of Astronomy, Harvard University, 60 Garden Street, Cambridge, MA 02138, USA

¹² Jet Propulsion Laboratory, California Institute of Technology, 4800 Oak Grove Drive, Pasadena, CA 91109, USA

¹³ NASA Goddard Space Flight Center, Greenbelt, MD 20771, USA

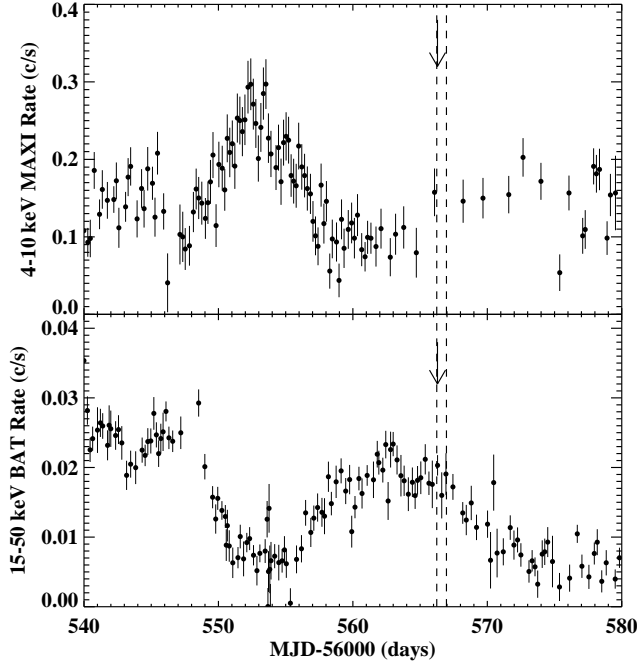


FIG. 1.— *MAXI* and *BAT* light curves with the time of the *NuSTAR* observations marked by the dashed lines. The arrow marks the time of the *Swift* observation.

the XRT observation lasted for two *Swift* orbits, the source was near the edge of the active area of the detector for the first orbit, and we produced an energy spectrum using only the second orbit, giving an exposure time of 1068 s. As this source has a relatively high column density, we used only grade 0 photons as this is the recommended procedure for high column density sources¹⁵. The spectrum was extracted from a circular region with a 20 pixel (47'') radius, and background was taken from a region far from the source. We obtained a source count rate in the 0.7–10 keV band of 17.7 c/s. For spectral fitting, we calculated a response matrix appropriate for grade 0 photons (file `swxwt0s6_20130101v015.rmf`) and used `xrtmkarf` with an exposure map to produce the ancillary response file.

All spectra were analyzed using XSPEC version 12.8 (Arnaud 1996). All fits were made assuming Verner et al. (1996) cross sections and Wilms et al. (2000) abundances. The spectra were binned such that the signal-to-noise ratio in each bin is 15σ . To better constrain the low energy spectrum, particularly the column density, we fit the *Swift* spectrum together with the *NuSTAR* spectra. Due to flux variations between the instruments, we added a multiplicative constant in each fit. We fixed the constant for the *NuSTAR* FPMA spectrum to unity and allowed the constants for the *NuSTAR* FPMB and *Swift* spectra to vary.

3. ANALYSIS AND RESULTS

4U 1728-34 is known to exhibit Type-1 X-ray bursts. Using the light curves made by the `nuproducts` FTOOL, we detected and removed four bursts in the *NuSTAR* data, each lasting about 20 s (Figure 2). No bursts were detected during the *Swift* observation. To check the stability of the energy spectrum during the observation, we looked at the hardness ratio, defined here as the count rate from 12-25 keV divided

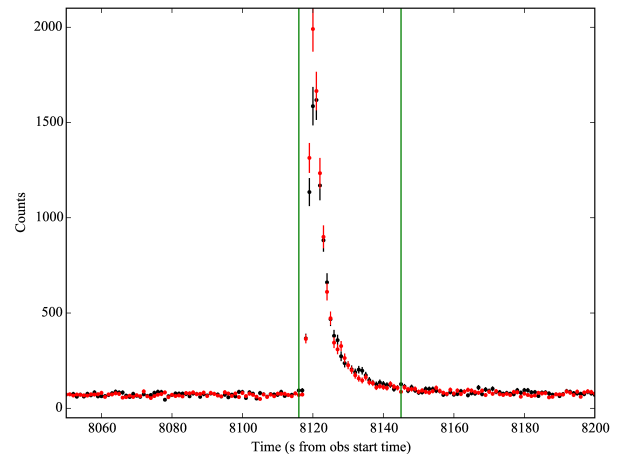
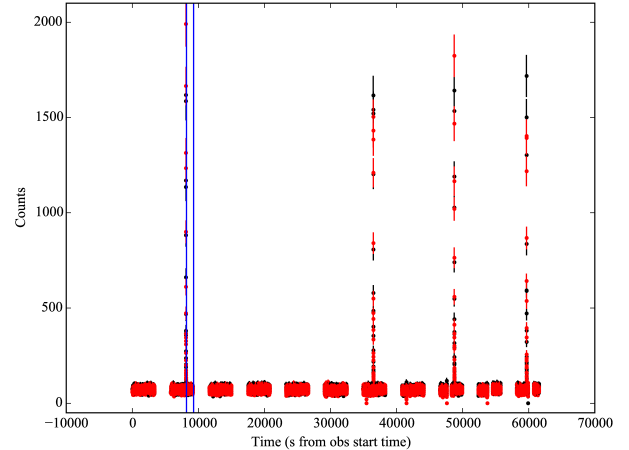


FIG. 2.— (a) The *NuSTAR* FPMA (black) and FPMB (red) light curve, including the four type 1 X-ray bursts. The time of the *Swift* observation is marked in blue. (b) A close-up of the first type 1 X-ray burst. The green lines indicate the data removed for spectral analysis.

by the count rate from 4.5-12 keV (Figure 3). The hardness ratio only changes slightly, softening gradually with time, indicating a fairly stable spectrum.

We first fit the combined *Swift* and *NuSTAR* continuum spectra similarly to Ng et al. (2010), with a model consisting of a neutral absorption component `tbabs`, a single temperature blackbody `bbbodyrad`, a disk blackbody `diskbb`, and a powerlaw component `cutoffpl`. This model takes into account thermal emission from the boundary layer between the neutron star surface and disk, thermal emission from the disk, and non-thermal emission from Comptonization. We found a blackbody temperature of 1.41 ± 0.01 keV, a disk blackbody temperature of 0.32 ± 0.02 keV, a photon index of 1.29 ± 0.05 , and a cutoff energy of 18.3 ± 0.7 keV (all errors are 90% confidence). This model fits most of the energy band fairly well ($\chi^2/\text{dof} = 1700/1257 = 1.35$), but there are significant residuals between 6-8 keV (Figure 4).

We added a Gaussian line to model the excess at ~ 6 keV. Leaving the line parameters free gives unphysical results (the line energy is at ≈ 5.7 keV with a width $\sigma \approx 1.6$ keV). Similarly to D’Aí et al. (2006) and Eggen et al. (2011), we limited the line width to $\sigma = 0.5$ keV, resulting in a line energy of 6.56 ± 0.05 keV and an equivalent width of 74 eV. The

¹⁵ see http://www.swift.ac.uk/analysis/xrt/digest_cal.php#abs

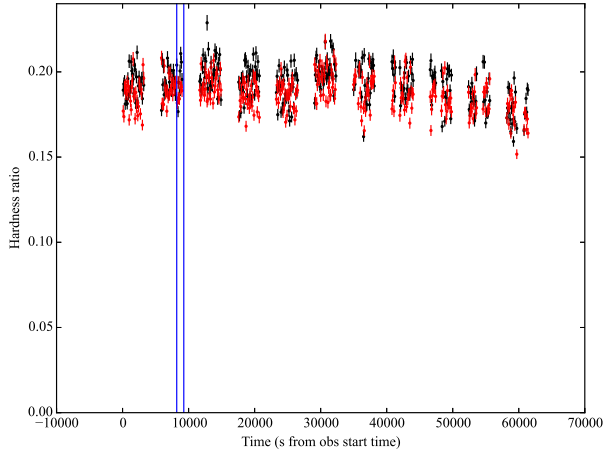


FIG. 3.— The hardness ratio throughout the *NuSTAR* observation, with *NuSTAR* FPMA in red and *NuSTAR* FPMB in black. The time of the *Swift* observation is marked in blue. The hardness ratio is defined as the count rate from 12-25 keV / the count rate from 4.5-12 keV.

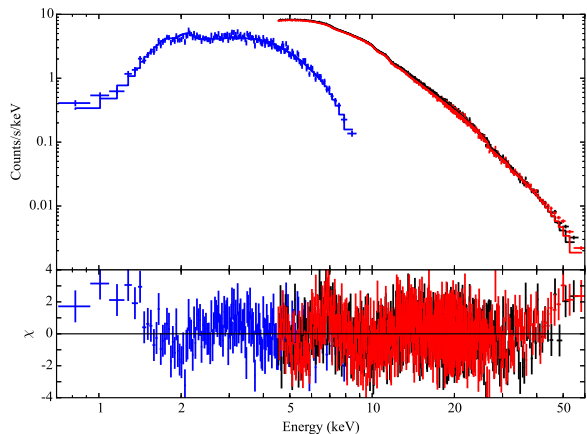


FIG. 4.— The 4.5-78.4 keV *NuSTAR* FPMA (black) and *NuSTAR* FPMB (red) spectra and the 0.7-10 keV *Swift* (blue) spectrum of 4U 1728-34, fit with the continuum model: disk blackbody + blackbody + power-law. The residuals between 6-8 keV indicate the presence of iron emission.

addition of a Gaussian significantly improved the fit, with a $\chi^2/\text{dof} = 1529/1253 = 1.22$. Moreover, the `diskbb` component became statistically insignificant, its exclusion from the fit resulting in $\Delta\chi^2 = 5$ and only slight changes to the other parameters. We continued our analysis without the `diskbb` component.

Having confirmed the presence of the iron line with the Gaussian model, we replaced this phenomenological model with a physical reflection model, `relionx` (Ross & Fabian 2005). The `relionx` model used here is a version of Ross & Fabian (2005) that assumes reflection of a power law with a high-energy exponential cutoff. To take relativistic blurring into account, we convolved `relionx` with `kerrconv` (Brenneman & Reynolds 2006).

The `relionx` parameters include the photon index and cutoff energy (tied to those of the `cutoffpl` component), the ionization ($\xi = L/nr^2$, or the ratio of the flux to the column density, where L is the luminosity, r is the distance, and

n is the column density), the iron abundance (A_{Fe}), and the flux. The `kerrconv` parameters include the compact object spin parameter, disk inclination, disk inner and outer radius, and inner and outer emissivity indices. The spin parameter $a \equiv cJ/GM^2 = 0.15$ (where J is angular momentum) can be calculated from previous measurements of the neutron star spin frequency, 363 Hz (Strohmayer et al. 1996), assuming a typical neutron star mass of $M = 1.4M_{\odot}$. We fixed the disk outer radius $R_{\text{out}} = 400R_{\text{ISCO}}$ (where R_{ISCO} is the radius of the innermost stable circular orbit) because the emissivity profile drops steeply with radius, causing the fits to be insensitive to the exact value of this parameter.

As it was difficult to constrain the emissivity when it was left free, we considered fits with $q = 1, 2, 3, 4$ and 5. We also considered a broken power law with the outer index fixed to 3, the inner index left free, and the break radius fixed to $25R_{\text{g}}$, but we were unable to constrain the inner index. As shown in Table 1, the changes in emissivity negligibly affect the χ^2 . Furthermore, the values for the inner radius are very similar across the models (other than $q = 1$, where the inner radius has very large error bars). As the parameters, particularly the inner radius, seem to be insensitive to the emissivity, we continued our analysis with the emissivity fixed at $q = 3$, consistent with a Newtonian geometry far from the neutron star.

Adding the reflection component (Figure 5) improves the fit over the Gaussian line model ($\chi^2/\text{dof} = 1430/1254 = 1.14$; $\Delta\chi^2 = 99$). Table 2 lists the best fit parameters for the relativistically blurred reflection model (model 1). We find an inclination of $\sim 37^\circ$, consistent with the lack of dips in the light curve which implies a low viewing angle. From the normalization of `tbodyrad`, we find a blackbody source radius of 1.4 km, consistent with thermal emission from the boundary layer. We find a higher column density, $N_{\text{H}} \sim 4.5 \times 10^{22} \text{ cm}^{-2}$, than what has been previously measured for this source ($N_{\text{H}} \sim 2.6 - 2.9 \times 10^{22} \text{ cm}^{-2}$, e.g. Di Salvo et al. 2000; Piraino et al. 2000; Narita et al. 2001; Eggen et al. 2011). To be consistent with past measurements, we fixed the column density to $2.9 \times 10^{22} \text{ cm}^{-2}$ (Figure 6; model 2 in Table 2). This significantly worsens the fit, resulting in a $\chi^2/\text{dof} = 1712/1255 = 1.36$ ($\Delta\chi^2 = 282$), yet does not cause a large change to the main parameter of interest, R_{in} .

Due to the proximity of 4U 1728-34 to the Galactic plane ($b = -0.15^\circ$), it is reasonable to consider the column density of molecular hydrogen. Galactic surveys indicate that at the position of 4U 1728-34, $N_{\text{H}_2} \sim 1.8 \times 10^{22} \text{ cm}^{-2}$ (Dame et al. 2001) and $N_{\text{H}_1} \sim 1.24 \times 10^{22} \text{ cm}^{-2}$ (Kalberla et al. 2005). Thus, the expected total column density is $N_{\text{H}_{\text{total}}} = N_{\text{H}_1} + 2N_{\text{H}_2} \sim 4.84 \times 10^{22} \text{ cm}^{-2}$, close to our measured value. We conclude that the model with the column density as a free parameter, which is a better fit to the data, is more correct. From this model, we find an upper limit for the disk inner radius $R_{\text{in}} \leq 1.77R_{\text{ISCO}}$, with the best value at $R_{\text{in}} = 1.00^{+0.77}_{-0}R_{\text{ISCO}}$.

We also fit only the iron line (4.5-8.5 keV) with the `relionx` model to consider the extent of the shape of the relativistic profile determined by the iron line as opposed to the broadband continuum. Because this spectrum with the data below 4.5 keV excluded is inadequate to measure the column density, we fixed $N_{\text{H}} = 2.9 \times 10^{22} \text{ cm}^{-2}$. The best fit parameters of this model are shown in Table 2 (model 3). Without the broadband spectrum, we were unable to constrain the continuum parameters. Many of the smearing parameters, however, are similar to those in models 1 and 2, most notably

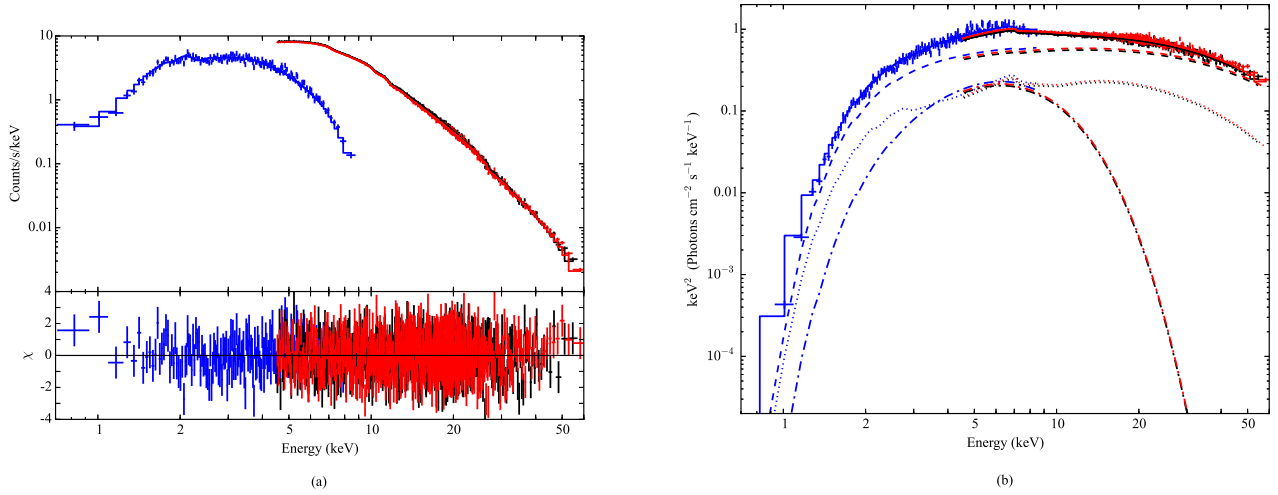


FIG. 5.— The 4.5–78.4 keV *NuSTAR* FPMA (black) and *NuSTAR* FPMB (red) spectra and the 0.7–10 keV *Swift* (blue) spectrum of 4U 1728–34, fit with the `reflionx` relativistically blurred reflection model (model 1). (a) Shows the residuals of the reflection model, specifically the lack thereof between 6–8 keV. (b) Shows the νF_ν plot with individual model components: blackbody (dashed and dotted), cutoff power-law (dashed), and `reflionx` (dotted).

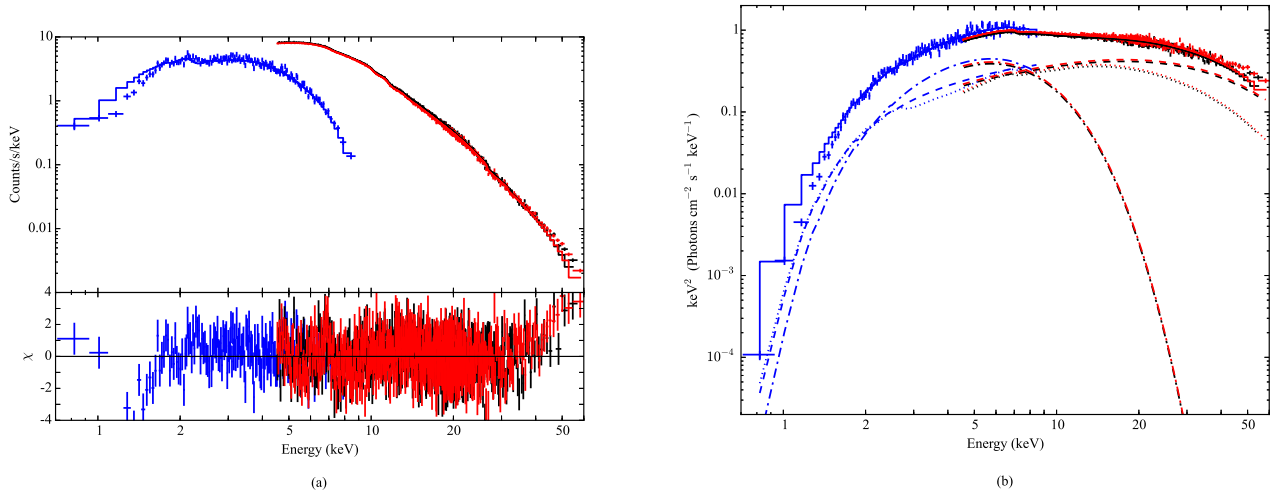


FIG. 6.— The 4.5–78.4 keV *NuSTAR* FPMA (black) and *NuSTAR* FPMB (red) spectra and the 0.7–10 keV *Swift* (blue) spectrum of 4U 1728–34, fit with the `reflionx` relativistically blurred reflection model where the column density is fixed to $2.9 \times 10^{22} \text{ cm}^{-2}$ (model 2). (a) Shows the residuals of the reflection model. (b) Shows the νF_ν plot with individual model components: blackbody (dashed and dotted), cutoff power-law (dashed), and `reflionx` (dotted).

the inner radius $R_{\text{in}} \leq 1.2R_{\text{ISCO}}$, indicating that much of the relativistic profile is determined by the iron line rather than the broadband continuum.

To verify that the *Swift* spectrum helps constrain the spectral shape, we fit only the *NuSTAR* data using the `reflionx` model (model 4 in Table 2). We fixed the column density to $2.9 \times 10^{22} \text{ cm}^{-2}$ as the *NuSTAR* data is unable to measure this parameter. Fitting only the *NuSTAR* spectrum with this model resulted in a $\chi^2/\text{dof} = 1256/1096 = 1.15$ and is statistically better than including the *Swift* data (model 3 in Table 2; $\chi^2/\text{dof} = 1712/1255 = 1.36$). However, without the low energy data from *Swift*, the column density cannot be well measured and thus the inaccuracy of fixing $N_{\text{H}} = 2.9 \times 10^{22} \text{ cm}^{-2}$ is not revealed in the fit statistics. Without the *Swift* spectrum, we find $R_{\text{in}} \leq 2.7R_{\text{ISCO}}$ as an upper limit for the inner radius (contrasting $R_{\text{in}} \leq 1.4R_{\text{ISCO}}$ found in model 3), indicating that the *Swift* spectrum is useful in evaluating the main parameter

of interest as well as the column density.

Mondal et al. (2016) have also analyzed this coordinated *NuSTAR* and *Swift* observation, fitting the data instead with `relxill`, another relativistically blurred reflection model (García et al. 2014). To compare to their results, we also fit the spectrum with `relxill`, and in addition replaced `cutoffpl` for the more physical `comptt`. The `relxill` parameters include the ionization, iron abundance, compact object spin parameter, disk inclination, disk inner and outer radius, and inner and outer emissivity indices. Again we fixed $R_{\text{out}} = 400R_{\text{ISCO}}$ and $a = 0.15$. Similarly to Mondal et al. (2016), we fixed $q_{\text{out}} = 3$ and left q_{in} free, but we were only able to find a lower limit on q_{in} . The `relxill` model is statistically similar to model 1 with a $\chi^2/\text{dof} = 1412/1250 = 1.13$, and the best fit parameters shown in Table 3 are comparable to those of model 1. In particular, the column density $N_{\text{H}} = 3.9 \times 10^{22} \text{ cm}^{-2}$ is considerably higher than past mea-

measurements and the inclination $i = 37^\circ$ is the same as model 1. We find an upper limit of $R_{\text{in}} \leq 2R_{\text{ISCO}}$ for the disk inner radius, with the best value at $R_{\text{in}} = 1.6 \pm 0.4$. This upper limit is close to our previous upper limit of $1.77R_{\text{ISCO}}$, but as it is slightly higher, we continue our analysis considering $R_{\text{in}} \leq 2R_{\text{ISCO}}$ as the upper limit for the disk inner radius.

With spin parameter value of $a = 0.15$, we calculate $1 R_{\text{ISCO}} = 5.5R_g$ (Bardeen et al. 1972). Assuming a typical neutron star mass of $1.4M_\odot$, we find an upper limit for the neutron star radius $R_{\text{NS}} \leq 2 \times 5.5R_g = 23$ km (Figure 8).

4. DISCUSSION

The unabsorbed flux extrapolated in the 0.1-100 keV energy range is $F \sim 6 \times 10^{-9}$ erg cm $^{-2}$ s $^{-1}$. Assuming a distance to the source of 5.1 kpc (Di Salvo et al. 2000; Galloway et al. 2003), we calculate a luminosity $L_{0.1-100} = 1.9 \times 10^{37}$ erg s $^{-1}$, corresponding to 8% of the Eddington luminosity, $L_{\text{EDD}} = 2.5 \times 10^{38}$ erg s $^{-1}$ (van Paradijs & McClintock 1994). We note that this value is around an average luminosity for 4U 1728-34 compared to previous observations. Di Salvo et al. (2000) measured $L_{0.1-100} = 2 \times 10^{37}$ erg s $^{-1}$. Others have used different energy ranges; for the sake of comparison, we re-calculate the unabsorbed flux and luminosity in different ranges. Egron et al. (2011) measured $L_{0.1-150} = 5 \times 10^{36}$ erg s $^{-1}$, in comparison to our value of $L_{0.1-150} = 1.9 \times 10^{37}$ erg s $^{-1}$. Piraino et al. (2000) measured $L_{0.2-50} = 3.7 \times 10^{37}$ erg s $^{-1}$, while we measure of $L_{0.2-50} \sim 1.7 \times 10^{37}$ erg s $^{-1}$. Ng et al. (2010) measured $L_{2-10} = 7.8 \times 10^{35}$ erg s $^{-1}$, compared to our measurement of $L_{2-10} \sim 6.6 \times 10^{36}$ erg s $^{-1}$.

With our upper limit on the accretion disk inner radius $R_{\text{in}} \leq 23$ km, we infer an upper limit on the neutron star magnetic field strength by equating the magnetic field pressure to the ram pressure of the accretion disk (Illarionov & Sunyaev 1975). We use the following relation:

$$R_{\text{in}} = 4 \times 10^8 B_{11}^{4/7} \dot{m}_{15}^{-2/7} M^{-1/7} \text{ cm} \quad (1)$$

where B_{11} is the magnetic field in units of 10^{11} G, \dot{m}_{15} is the mass accretion rate in units of 10^{15} g s $^{-1}$, and M is the neutron star mass in solar masses. We calculate the mass accretion rate from the luminosity given above with the relation $L = \eta \dot{m} c^2$, where $\eta = GM/Rc^2$. Assuming $M = 1.4M_\odot$, we find $B \leq 2 \times 10^8$ G.

We compare our results with those obtained for other neutron star LMXBs also observed with *NuSTAR*. Miller et al. (2013) found that Serpens X-1, a persistent source, has a disk extending almost to the ISCO when observed at a luminosity of $L \sim 0.44L_{\text{EDD}}$. From their measured values of L and R_{in} , we estimate $B \leq 2.2 \times 10^8$ G. Degenaar et al. (2015) found that 4U 1608-52, a transient source with a spin frequency of 620 Hz, also has a disk extending close to the ISCO when observed at a luminosity of $L \sim 0.02L_{\text{EDD}}$; we estimate $B \leq 1.2 \times 10^8$ G. Aql X-1, also a transient observed by King et al. (2016) at a luminosity of $L \sim 0.08L_{\text{EDD}}$, has a truncated disk ($R_{\text{in}} \sim 15R_g$), a spin frequency of 550 Hz, and a magnetic field $B \leq 5 \pm 2 \times 10^8$ G.

According to White & Zhang (1997), a higher spin frequency should imply a lower magnetic field: with a low magnetic field, the disk can extend deeper into the potential, spinning up the neutron star. While it is consistent that the disk extends closer to the ISCO in the above sources with lower

magnetic fields, the correlation between spin frequency and magnetic field is not always followed. While 4U 1608-52 has the highest spin frequency and lowest magnetic field, Aql X-1 has both a higher spin frequency and a higher magnetic field than 4U 1728-34. (The spin frequency of Serpens X-1 is unknown, so we leave it out of this comparison.)

It is likely that this discrepancy is due to the expected variability in LMXB spin periods and magnetic fields. It is possible, however, that the discrepancy is real, in which case we consider the effects of magnetic field screening (Cumming et al. 2001) as an explanation. Magnetic field screening is a process by which the accreting matter becomes magnetized slowly compared to the accretion rate, causing the field implied by equating the pressures to be orders of magnitude smaller than the true field of the neutron star. Because Aql X-1 is a transient, we consider the possibility that the magnetic field emerges during quiescence and is not screened immediately after the outburst begins. The time it takes for the magnetic field to become significantly screened depends on accretion rate; for an accretion rate of $0.08L_{\text{EDD}}$, the field will be screened by one order of magnitude five days or less after the outburst began (Cumming 2008). The observation of Aql X-1 occurred less than five days after the outburst began; hence it is possible that Aql X-1 is not fully screened (though a better estimate of the screening timescale could further support, or refute, this hypothesis). This possibility provides an explanation for the low spin frequency and magnetic field of 4U 1728-34 as compared to Aql X-1.

Our upper limit for the radius of the neutron star, $R_{\text{NS}} \leq 23$ km, assumes that the star extends all the way to the disk. In that case, accretion onto the neutron star is straightforward. Because the magnetic field is relatively low, it is possible that the material is getting to the neutron star via a magnetic gate (Lamb et al. 1977). Due to chaotic accretion on the stellar surface, type II X-ray bursts are expected in the magnetic gate model, yet are not exhibited in 4U 1728-34. Instead, the material could be channeled along the magnetic field lines to the poles (Lamb et al. 2009). This scenario would cause a hot spot on the magnetic pole. However, it is possible that the magnetic axis is aligned with the rotation axis as 4U 1728-34 does not emit regular pulsations.

5. SUMMARY

We have analyzed the persistent emission of neutron star LMXB 4U 1728-34 using a concurrent *NuSTAR* and *Swift* observation. By fitting the continuum with a power law and thermal components, we find clear evidence of an Fe $K\alpha$ line in the spectrum of 4U 1728-34. With a relativistically blurred reflection model, we find an upper limit to the accretion disk inner radius, and thus the neutron star radius, of $R_{\text{NS}} \leq 23$ km. From this, we infer the upper limit on the magnetic field of the neutron star to be $B \leq 2 \times 10^8$ G.

We thank Michael Parker and Andy Fabian for the particular version of the `reflionx` model used in this analysis. We thank Kristin Madsen for her help identifying the calibration issue in the *NuSTAR* data between 3-4.5 keV. JC thanks ESA/PRODEX for financial support. This work is based on data from the *NuSTAR* mission, a project led by the California Institute of Technology, managed by the Jet Propulsion Laboratory, and funded by NASA.

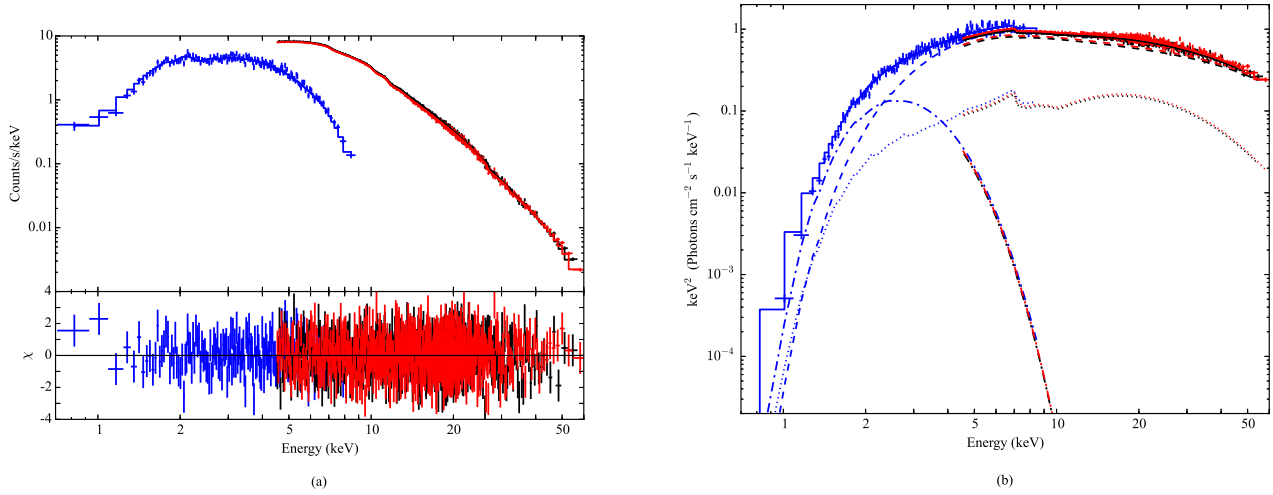


FIG. 7.— The 4.5–78.4 keV *NuSTAR* FPMA (black) and *NuSTAR* FPMB (red) spectra and the 0.7–10 keV *Swift* (blue) spectrum of 4U 1728–34, fit with `relxill` (model 5). (a) Shows the residuals of the reflection model. (b) Shows the νF_ν plot with individual model components: blackbody (dashed and dotted), `comptt` (dashed), and `relxill` (dotted).

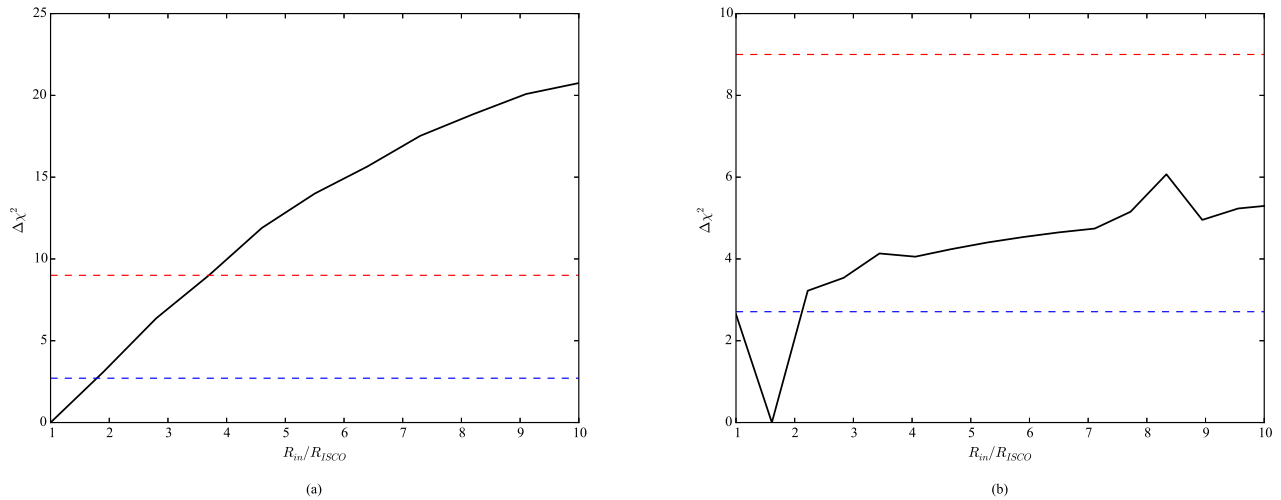


FIG. 8.— The change in χ^2 versus the change in inner radius, showing that the model is consistent with the disk extending to the ISCO. The dashed blue line marks 90% confidence and the dashed red line marks 99.7% confidence (3σ). (a) Shows the results of the `reflionx` model (model 1). (b) Shows the results of the `relxill` model (model 5).

REFERENCES

- Arnaud, K. A., 1996, in *Astronomical Data Analysis Software and Systems V*, ed. G. H. Jacoby, J. Barnes, Vol. 101, Astronomical Society of the Pacific Conference Series, 17
- Bardeen, J. M., Press, W. H., & Teukolsky, S. A. 1972, *ApJ*, 178, 347
- Brenneman, L. W., & Reynolds, C. S. 2006, *ApJ*, 652, 1028
- Burrows, D. N., Hill, J. E., Nousek, J. A., et al. 2005, *Space Science Reviews*, 120, 165
- Cackett, E. M., Miller, J. M., Ballantyne, D. R., et al. 2010, *ApJ*, 720, 205
- Cumming, A., 2008, *AIP Conference Proceedings*, 1068
- Cumming, A., Zweibel, E., & Bildsten, L. 2001, *ApJ*, 557, 958
- D’Ai, A., Di Salvo, T., Iaria, R., et al. 2006, *A&A*, 448, 817
- Dame, T. M., Hartmann, D., & Thaddeus, P. 2001, *ApJ*, 547, 792
- Degenaar, N., Miller, J. M., Chakrabarty, D., et al. 2015, *MNRAS*, 451, L85
- Di Salvo, T., Iaria, R., Burderi, L., & Robba, A. 2000, *ApJ*, 542, 1034
- Egron, E., Di Salvo, T., Burderi, L., et al. 2011, *A&A*, 530, 7
- Fabian, A. C., Rees, M. J., Stella, L., & White, N. E. 1989, *MNRAS*, 238, 729
- Galloway, D. K., Psaltis, D., Chakrabarty, D., & Munro, M. P. 2003, *ApJ*, 590, 999
- Galloway, D. K., Yao, Y., Marshall, H., Misanovic, Z., & Weinberg, N. 2010, *ApJ*, 724, 417
- García, J., Dauser, T., Lohfink, A., et al. 2014, *ApJ*, 782, 76
- Gehrels, N., Chincarini, G., Giommi, P., et al. 2004, *ApJ*, 611, 1005
- Harrison, F. A., Craig, W. W., Christensen, F. E., et al. 2013, *ApJ*, 770, 103
- Hasinger, G., & van der Klis, M. 1989, *A&A*, 225, 79
- Illarionov, A. F., & Sunyaev, R. A. 1975, *A&A*, 39, 185
- Kalberla, P. M. W., Burton, W. B., Hartmann, D., et al. 2005, *A&A*, 440, 775
- King, A. L., Tomsick, J. A., Miller, J. M., et al. accepted 2016
- Lamb, F. K., Boutloukos, S., Van Wassenhove, S., et al. 2009, *ApJ*, 706, 417
- Lamb, F. K., Fabian, A. C., Pringle, J. E., & Lamb, D. Q. 1977, *ApJ*, 217, 197
- Lattimer, J. M., & Prakash, M. 2007, *Phys.Rep.* 442, 109
- Lewin, W. H. G., Clark, G., & Doty, J. 1976, *IAU Circular*, 2922
- Miller, J. M., 2007, *ARA&A*, 45, 441
- Miller, J. M., Parker, M. L., Fuerst, F., et al. 2013, *ApJ*, 779, L2
- Mondal, A. S., Pahari, M., Dewangan, G. C., Misra, R., & Raychaudhuri, B. 2016, submitted to *MNRAS* (arxiv:1604.04366)
- Narita, T., Grindlay, J. E., & Barret, D. 2001, *ApJ*, 547, 420

- Ng, C., Diaz Trigo, M., Cadolle Bel, M., & Migliari, S. 2010, *A&A*, 522, 25
- Piraino, S., Santangelo, A., & Kaaret, P. 2000, *A&A*, 360, L35
- Reynolds, C. S., & Nowak, M. A. 2003, *Phys.Rep.*, 377, 389
- Ross, R. R., & Fabian, A. C. 2005, *MNRAS*, 358, 211
- Seifina, E., & Titarchuk, L. 2011, *ApJ*, 738, 128
- Strohmayer, T. E., Zhang, W., Swank, J. H., et al. 1996, *ApJ*, 469, L9
- Tarana, A., Belloni, T., Bazzano, A., Méndez, M., & Ubertini, P. 2011, *MNRAS*, 416, 873
- van Paradijs, J., & McClintock, J. E. 1994, *A&A*, 290, 133
- Verner, D. A., Ferland, G. J., Korista, K. T., & Yakovlev, D. G. 1996, *ApJ*, 465, 487
- White, N. E., & Zhang, W. 1997, *ApJ*, 490, L87
- Wilms, J., Allen, A., & McCray, R. 2000, *ApJ*, 542, 914

TABLE 1
SPECTRAL PARAMETERS WITH VARIED EMISSIVITY USING THE REFLIONX MODEL

Model	Parameter ^a	Units	$q = 1$	$q = 2$	$q = 3$	$q = 4$	$q = 5$	q broken
constant	FPMA	–	1 ^b					
	FPMB	–	1.05 ± 0.002	1.05 ± 0.002	1.05 ± 0.002	1.05 ± 0.002	1.05 ± 0.002	1.05 ± 0.002
	XRT	–	1.12 ± 0.01	1.12 ± 0.01	1.15 ± 0.01	1.13 ± 0.01	1.13 ± 0.02	1.12 ± 0.02
tbabs	N_{H}^{c}	10^{22} cm^{-2}	4.6 ± 0.1	4.5 ^{+0.1} _{-0.2}	4.5 ± 0.1	4.4 ± 0.1	4.4 ± 0.1	4.4 ± 0.1
bbodyrad	kT	keV	1.54 ± 0.02	1.69 ^{+0.03} _{-0.09}	1.53 ^{+0.02} _{-0.05}	1.52 ± 0.04	1.53 ± 0.04	1.49 ^{+0.06} _{-0.01}
cutoffpl	norm	$R_{\text{km}}^2/D_{10\text{kpc}}^2$	6.26 ^{+1.4} _{-0.5}	4.2 ^{+0.7} _{-0.4}	7.9 ^{+2.6} _{-0.7}	8.5 ± 2	7.7 ^{+3.3} _{-1.7}	9.4 ^{+1.7} _{-2.1}
	Γ	–	1.52 ^{+0.04} _{-0.03}	1.51 ^{+0.02} _{-0.01}	1.54 ^{+0.04} _{-0.05}	1.52 ^{+0.05} _{-0.02}	1.51 ± 0.05	1.52 ± 0.04
HighECut	norm	Photons $\text{keV}^{-1} \text{ cm}^{-2} \text{ s}^{-1}$ at 1keV	26 ⁺³ ₋₁	26 ⁺² ₋₄	25 ± 2	25 ⁺² ₋₃	26 ⁺³ ₋₂	26 ⁺³ ₋₁
	q_{in}	–	1 ^b	2 ^b	3 ^b	4 ^b	5 ^b	> 5.4
kerrconv	q_{out}	–	1 ^b	2 ^b	3 ^b	4 ^b	5 ^b	3 ^b
	a	–	0.15 ^b					
reflionx	Incl.	deg.	35 ⁺¹³ ₋₅	19 ⁺⁸ ₋₄	37 ⁺¹ ₋₂	37 ⁺² ₋₄	39 ⁺² ₋₄	40 ⁺¹ ₋₃
	R_{in}	ISCO	3.2 ^{+3.45} _{-2.2}	1.0 ^{+0.56} ₋₀	1.0 ^{+0.77} ₋₀	1.1 ^{+0.50} _{-0.1}	1.1 ^{+0.48} _{-0.1}	1.2 ^{+0.4} ₋₀
	R_{out}	ISCO	400 ^b					
	ξ	erg cm s^{-1}	3142 ⁺⁹⁸⁷ ₋₃₀₂	4564 ⁺²⁰⁰⁰ ₋₁₅₅₆	796 ⁺⁷⁹⁸ ₋₂₂₉	984 ⁺⁷²² ₋₄₇₂	1208 ⁺⁵⁵⁹ ₋₅₃₂	1135 ⁺³⁵⁰ ₋₂₆₅
	A_{Fe}	–	0.22 ± 0.1	0.46 ^{+0.01} _{-0.68}	0.19 ± 0.1	0.17 ^{+0.06} _{-0.04}	0.19 ^{+0.07} _{-0.08}	0.14 ± 0.01
norm	10^{-6}	1.3 ^{+0.3} _{-0.2}	0.9 ^{+0.3} _{-0.2}	3.8 ^{+2.6} _{-1.4}	3.6 ^{+2.3} _{-0.6}	3.2 ^{+1.8} _{-0.9}	4.1 ^{+1.3} _{-1.2}	
χ^2/dof	–	–	1431/1254	1427/1254	1430/1254	1427/1254	1425/1254	1422/1253

^aThe errors on the parameters are 90% confidence.

^bThese parameters were fixed.

^cThe column density is calculated assuming Wilms et al. (2000) abundances and Verner et al. (1996) cross sections.

TABLE 2
SPECTRAL PARAMETERS VARYING THE COLUMN DENSITY AND THE ENERGY BAND USING REFLIONX

Model	Parameter ^a	Units	Model 1 Full band	Model 2 N_{H} fixed	Model 3 4.5-8.5 keV	Model 4 <i>NuSTAR</i> only
constant	FPMA	–	1 ^b	1 ^b	1 ^b	1 ^b
	FPMB	–	1.05 ± 0.002	1.05 ± 0.002	1.05 ± 0.003	1.05 ± 0.002
	XRT	–	1.12 ± 0.02	1.15 ± 0.01	1.15 ± 0.03	–
tbabs	N_{H}^{c}	10^{22} cm^{-2}	4.5 ± 0.1	2.9 ^b	2.9 ^b	2.9 ^b
bbodyrad	kT	keV	1.53 ^{+0.02} _{-0.05}	1.42 ± 0.01	–	1.45 ^{+0.06} _{-0.03}
cutoffpl	norm	$R_{\text{km}}^2/D_{10\text{kpc}}^2$	7.9 ^{+2.6} _{-0.7}	20.6 ^{+0.8} _{-0.4}	–	10.8 ± 1.8
	Γ	–	1.54 ^{+0.04} _{-0.05}	1.0 ^{+0.02} _{-1.0}	2.21 ± 0.02	1.69 ± 0.08
HighECut	norm	Photons $\text{keV}^{-1} \text{ cm}^{-2} \text{ s}^{-1}$ at 1keV	25 ± 2	18.0 ^{+0.6} _{-0.1}	24.384 ^{+0.012} _{-0.004}	36 ⁺⁶ ₋₅
	q	–	3 ^b	3 ^b	3 ^b	3 ^b
kerrconv	a	–	0.15 ^b	0.15 ^b	0.15 ^b	0.15 ^b
	Incl.	deg.	37 ⁺¹ ₋₂	29 ⁺³ ₋₂	34.31 ^{+0.01} _{-0.22}	33 ⁺³ ₋₂
reflionx	R_{in}	ISCO	1.0 ^{+0.77} _{-1.0}	1.0 ^{+0.44} _{-1.0}	1.0 ^{+0.2} _{-1.0}	1.7 ^{+1.0} _{-0.7}
	R_{out}	ISCO	400 ^b	400 ^b	400 ^b	400 ^b
	ξ	erg cm s^{-1}	796 ⁺⁷⁹⁸ ₋₂₂₉	995 ⁺³⁰ ₋₆₂	581 ⁺¹⁰ ₋₉	909 ⁺³³⁷ ₋₁₈₉
norm	A_{Fe}	–	0.19 ± 0.1	0.09 ± 0.01	0.059 ^{+0.012} _{-0.004}	0.07 ^{+0.07} _{-0.01}
	10^{-6}	10^{-6}	3.8 ^{+2.6} _{-1.4}	3.3 ^{+0.4} _{-0.2}	77.8 ^{+31.5} _{-0.8}	8.8 ^{+4.2} _{-5.6}
$\Omega/2\pi$	–	–	0.43	0.76	–	–
χ^2/dof	–	–	1430/1254	1712/1255	269/232	1256/1096

^aThe errors on the parameters are 90% confidence.

^bThese parameters were fixed.

^cThe column density is calculated assuming Wilms et al. (2000) abundances and Verner et al. (1996) cross sections.

TABLE 3
SPECTRAL PARAMETERS USING RELXILL

Model	Parameter ^a	Units	Value
constant	FPMA	–	1 ^b
	FPMB	–	1.05 ± 0.002
	XRT	–	1.15 ± 0.02
tbabs	N_{H}^{c}	10^{22}cm^{-2}	$3.9^{+0.4}_{-0.3}$
bbody	kT	keV	$0.49^{+0.06}_{-0.05}$
	norm	$L_{10^{39} \text{ergs/s}} / D_{10 \text{kpc}}^2$	$0.007^{+0.002}_{-0.001}$
comptt	kT_{seed}	keV	$1.13^{+0.05}_{-0.03}$
	kT_e	keV	15^{+5}_{-3}
	optical depth	–	$1.6^{+0.3}_{-0.6}$
relxill	norm	–	$0.022^{+0.002}_{-0.007}$
	q_{in}	–	> 4
	q_{out}	–	3 ^b
	a	–	0.15 ^b
	Incl.	deg.	37^{+6}_{-2}
	R_{in}	ISCO	1.6 ± 0.4
	R_{out}	ISCO	400 ^b
	$\log \xi$	–	$3.0^{+0.1}_{-2.1}$
	A_{Fe}	–	0.8 ± 0.1
	norm	10^{-3}	$1.2^{+1}_{-0.2}$
χ^2/dof	–	–	1412/1250

^aThe errors on the parameters are 90% confidence

^bThese parameters were fixed

^cThe column density is calculated assuming Wilms et al. (2000) abundances and Verner et al. (1996) cross sections.